IEEE Access
Multidisciplinary | Rapid Review | Open Access Journal

Received 13 July 2022, accepted 22 July 2022, date of publication 1 August 2022, date of current version 10 August 2022.

Digital Object Identifier 10.1109/ACCESS.2022.3195493

APPLIED RESEARCH

A Two-Step Control Approach for Torque Ripple and Vibration Reduction in Switched Reluctance Motor Drives

MARCIO L. M. KIMPARA[1], (Member, IEEE), RENATA R. C. REIS[1], (Student Member, IEEE), LUIZ E. B. DA SILVA[2], (Senior Member, IEEE), JOAO O. P. PINTO[3], (Senior Member, IEEE), AND BABAK FAHIMI[4], (Fellow, IEEE)

[1]Electrical Engineering Department, Federal University of Mato Grosso do Sul, Campo Grande 79070-900, Brazil
[2]Electrical Engineering Department, Federal University of Itajubá, Itajubá 37500-903, Brazil
[3]Oak Ridge National Laboratory, Oak Ridge, TN 37831, USA
[4]Department of Electrical and Computer Engineering, The University of Texas at Dallas, Richardson, TX 75080, USA

Corresponding author: Marcio L. M. Kimpara (marcio.kimpara@gmail.com)

ABSTRACT The objective of this work is to reduce the torque ripple and vibration in Switched Reluctance Motor (SRM) drives. To achieve such a goal, a two-step approach is proposed. In the first step, the reference current is profiled using an optimization method, aimed to reduce the torque pulsation. In the second, the optimum current profile is applied to the SRM through an adaptive hysteresis band controller to actively cancel the radial vibration. The proposed technique uses an optimization procedure based on the Field Reconstruction Method (FRM) and Non-Derivative Optimization Method to find the optimal current profile that mitigates the torque pulsation, however, the investigation has shown that the proposed excitation leads to a higher radial vibration, which has been mitigated by using an adaptive hysteresis band controller. The theoretical basis for the proposed approach is initially presented, followed by system modeling and simulation. In addition, experimental verification has been conducted using an 8/6 SRM to show the feasibility of the proposed approach. The proposed method alleviates the acoustic noise and torque pulsation in SRM and offers an effective step towards the prevalent use of SRM in a wide range of applications.

INDEX TERMS Motor drives, switched reluctance motor, torque ripple, vibration, optimization.

I. INTRODUCTION

Switched reluctance machine presents a simple and rugged structure, with no permanent magnet or electrical excitation on the rotor. This feature provides advantages such as high efficiency, low cost, high power to weight ratio, wide speed range, and suitable conditions for operating under harsh environments [1]. Despite these attractive features, SRMs are not widely used in industrial applications due to their high levels of both torque pulsation and vibration/acoustic noise, when compared to their traditional counterparts.

For many years, these shortcomings have restricted the use of SRM drives in a multitude of applications. More recently, SRMs have been used for electric propulsion and applications, such as vacuum cleaners [2], [3]. Nevertheless, applications such as precision tooling, robotics, home appliances, or electrically assisted power steering, still need improved drive control to achieve the high-performance requirements.

Low acoustic noise is often desired, mainly in home appliances, meanwhile, the torque ripple leads to problems such as mechanical wear-out, mechanical vibrations, and speed oscillations. The attempt to overcome the adverse features of SRM, combined with the technological advancements in motor drives, has been the driving factor for many research projects, including optimal magnetic design and/or advanced control methodologies. However, if the motor is already built, the improvements are only possible by applying an appropriate control strategy.

The associate editor coordinating the review of this manuscript and approving it for publication was Zhuang Xu.

Among the proposed approaches, current profiling algorithms are effective in reducing the torque ripple. This family of controls consider SRM as a current to torque transducer with nonlinear mapping. To determine the optimal current profile, different techniques have been reported in the literature. A low torque ripple response under current-controlled operation, accomplished by profiling the phase current waveform has been covered in [4]. In [5], an appropriate phase current profile is obtained by using B-spline neural networks. Authors in [6] and [7] have modified the current shape for operating in the high-speed region with reduced torque ripple by employing numerical simulations. In [8], a dynamic current profiling system is proposed using sense coils. However, besides being an invasive method, additional signal processing with filters is required. In [9], the torque ripple minimization is accomplished in three steps, by combining machine design and control algorithms. In [10], a variable flux direct torque control (VF-DTC) is proposed to reduce the torque ripple. Albeit the dynamic response was found to be improved with this method, the relationship between the reference flux linkage and the reference torque must be properly tuned.

Similarly, the torque sharing function (TSF) method has been recently investigated as a powerful technique to minimize the torque ripple in SRMs [11], [12]. Nevertheless, analytical TSF methods essentially use the desired load torque, the rotor position, and a torque sharing function (linear, cubic, sinusoidal) to obtain the reference torque, which is applied in a torque-to-current converter to derive the reference current, i.e., the TSF method indirectly shapes the current waveform.

Accordingly, an analysis of the results found in different researches in the literature reveals that the obtained optimized phase current profile exhibits some similarities, regardless of the method employed. However, most of the previous research studies do not investigate the effects of the modified current waveform on the structural response of the motor. Consequently, the improvement of torque ripple performance of the SRM might worsen the radial vibration/acoustic noise levels, which are already significant in such motors.

Authors in [13]–[15] investigated current profiles with the aim of reducing torque ripple and radial vibration simultaneously. However, to suppress the vibration, the current profile is derived through shaping the radial forces, which might also affect the tangential component of the force, hence penalizing the torque generation. In general, the control methods tend to use current profiles (as an end result) to smooth the torque profile, however, either the average torque is reduced by applying less current when torque exhibits its peak value or the current magnitude is boosted during the commutation to preserve the average torque. The unintended consequence of the latter is that the outgoing phase will face substantially larger radial forces that in turn will ignite a more severe radial acceleration of the stator body.

This paper presents a novel two-step control approach for torque ripple reduction while preventing the rise of vibration in SRM drives. Firstly, the torque ripple reduction is achieved using an optimum reference current profile obtained through the Field Reconstruction Method-based model [16]. Subsequently, the principle of active vibration cancellation (AVC) is incorporated into the optimized current profile by adapting the hysteresis band in the current controller. The present paper is set apart from the existing body of work in that it simultaneously mitigates the torque pulsation and radial acceleration of the stator. The adaptive hysteresis band essentially controls the switching instants enhancing the effects of active cancellation without penalizing the average torque. This will not only reduce the radial vibration of the stator frame during turn-off process but also reduces the torque pulsation and its undesirable impact on bearing, end plates and tangential vibration of the stator. After the two-step optimization, the obtained current profile led the motor to operate with 42% less torque oscillation while the vibration is kept under control. All the experimental tests were accomplished using a 2 kW 8/6 SRM driven by an asymmetric bridge converter.

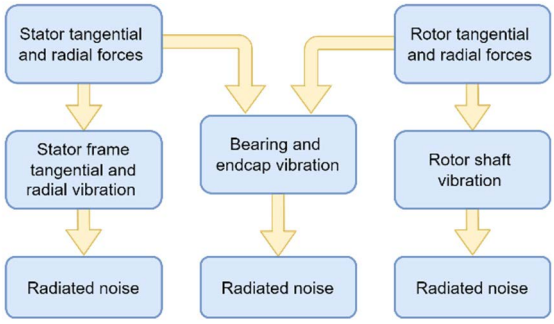

FIGURE 1. Origins of vibration and noise in SRM drives.

II. THE VIBRATION MECHANISM AND ACOUSTIC NOISE GENERATION IN SRM DRIVES

The SRM has an explicit double saliency structure and its principle of operation relies on magnetizing the stator poles when the rotor moves from an unaligned position towards an aligned one, giving rise to the electromagnetic attraction force. This force can be divided into two components, namely, the tangential force and radial force. Both components of the electromagnetic force can cause vibrations in different ways.

While contributing to the output torque, the tangential forces that are acting on the corner tips of the stator poles at the verge of overlap with rotor poles initiate a tangential motion in the stator frame. This tangential motion is consequently combined with a centripetal motion during the turn-off process, where radial forces exhibit very large magnitudes, triggering substantial vibration, and hence, acoustic noise. The tangential vibration mode of the stator and rotor poles can occur at frequencies within the range of human hearing, depending on the pole height [17]. Moreover, the transmission of magnetic forces through the shaft and end plates to the inner and outer races of the bearing will apply strong forces to the bearing that can initiate additional vibration [18]. Fig. 1 illustrates the main sources of vibration/noise in SRM drives.

TABLE 1. SRM parameters.

Parameter	Unit	Value
Phases	-	4
Pole configuration	-	8/6
Rated power	[kW]	2
Rated speed	[rpm]	6000
Stack length	[mm]	70.2
Stator outer diameter	[mm]	140
Rotor outer diameter	[mm]	79.4
Phase resistance	[mΩ]	12
Magnetic material	-	M-19
Turns per pole	-	8

Apart from that, SRMs exhibit high levels of torque pulsation due to the sequential nature of stator phase excitation and the highly non-linear torque variation with respect to the rotor position. Although torque pulsation mainly contributes to speed pulsation in low inertia systems and at relatively lower speeds, a high level of torque ripple will also lead to acoustic noise. Therefore, to achieve a low-noise SRM drive, both the torque ripple and radial vibration should be reduced [19].

III. SRM MODEL BASED ON THE FRM

To achieve the torque ripple and vibration reduction, the proposed control approach uses optimization algorithms that are based on the magnetic model of the SRM. Numerical methods, such as the well-known Finite Element (FE), have been widely applied to handle the nonlinear characteristics of the SRM. Nevertheless, the shortcoming of FE models is the solution time, i.e., depending on the granularity of the mesh, a high computation time is required.

In this paper, the Field Reconstruction Method (FRM), which has been proven to be effective and accurate as reported in [20] and [21], was used. This method is a fast-modeling process for electric machines in which a minimal set of magneto-static field solutions are used as the basis functions to determine the distribution of the electromagnetic flux density for an arbitrary excitation condition. The advantage of this approach is that the time processing is drastically shortened.

This section briefly describes the FRM procedure applied to the target motor whose main parameters are given in Table 1. Fig. 2 shows the SRM modeled in ANSYS Maxwell. The FE magneto-static solution for B_n (a normal component of the flux density) and B_t (a tangential component of the flux density) are sampled on a contour in the middle of the air gap. The applied current during this process is deemed as a basis value (i_b), and the magneto-static simulation is performed for the same basis current at different rotor positions, spanning from an unaligned to an aligned position. These solutions are treated as basis functions ($h\,(i_b, \theta_r)$)and are stored in look-up tables. According to the FRM fundamentals, the basis functions are then used to obtain (reconstruct) the flux distribution for any other excitation current by utilizing expressions (1) and (2) [20].

$$B_n\,(i_a, \theta_d) = \frac{i_a}{i_b}.h_n\,(i_b, \theta_d) \tag{1}$$

$$B_t\,(i_a, \theta_d) = \frac{i_a}{i_b}.h_t\,(i_b, \theta_d) \tag{2}$$

where:

B_n, B_t Normal and tangential components of flux density $\vec{B}$

i_b Base current (applied to obtain the basis functions)

θ_d Desired rotor position

i_a Arbitrary current excitation

$h_n\,(i_b, \theta_r)$

$h_t\,(i_b, \theta_r)$ Basis functions for each rotor position θ_r

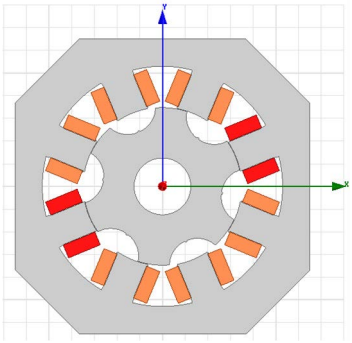

FIGURE 2. 2D cross-section of the 8/6 SRM in Maxwell/ANSYS.

Due to the void of permanent magnet and coil windings in the rotor of SRM, the FRM model is only represented by these two equations. Notably, the basis functions record the functional form of the flux density components, while the ratio between the currents modulates the magnitude of the flux density components. To account for saturation, [18] has presented a saturation multiplier coefficient. However, the machine under study presents a wide linear region in the flux linkage curve; thus, the saturation effects are negligible for the tested operation condition.

If the flux density $\vec{B}$ is known, further analysis, such as forces and torque, can be exploited using the Maxwell stress tensor [22]:

$$f_t = \frac{(B_n.B_t)}{\mu_0} \tag{3}$$

$$f_n = \frac{\left(B_n^2 - B_t^2\right)}{2\mu_0} \tag{4}$$

$$T = \int_{\Gamma} f_t.R.L_z dl \tag{5}$$

where μ_0 is the permeability of air, R is the radius of contour Γ in the airgap, and L_Z stands for the machine stack length.

To validate the FRM model, Fig. 3 shows the comparison between the flux density in normal and the tangential directions obtained through FE and FRM. The basis functions were extracted by applying 5 A. As shown by the error plot in Fig. 3, the flux distribution when the stator is excited

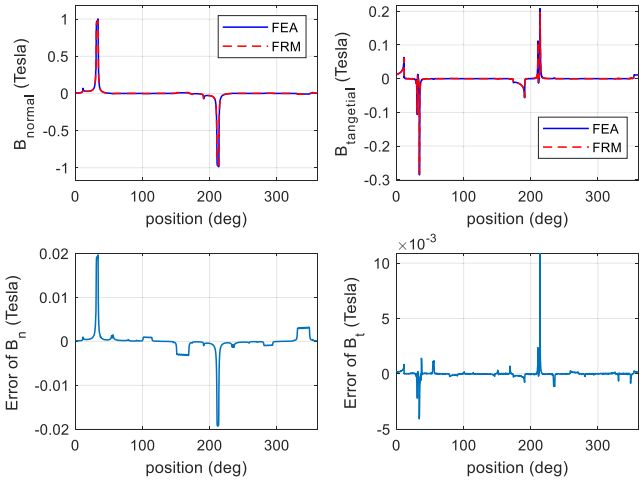

FIGURE 3. Comparison between FEA and FRM in obtaining the flux density components in the air gap for an arbitrary rotor position (10 degrees) and phase current excitation (23 A).

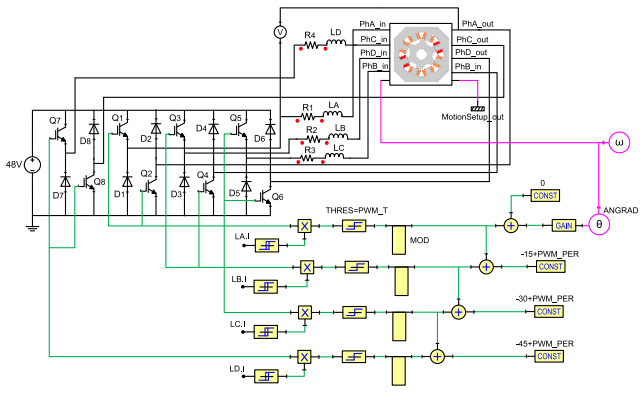

FIGURE 4. SRM drive co-simulation.

with 23 A at the rotor position $\theta_r = 10°$ given by the FE simulation and the FRM, are in good agreement. When analyzing the computational time, the advantage of FRM stands out. While the FE simulation took 2 minutes to calculate the flux distribution for this position and excitation (depicted in Fig. 3), the FRM simulation took less than a second with the same computational platform.

IV. FIRST-STEP: TORQUE RIPPLE MITIGATION

In the absence of saturation, the magnitude of torque generated in each phase is proportional to the rate of change of inductance and the square of the phase current, which is controlled by the converter and the torque control scheme. The torque polarity changes according to the inductance slope [23]:

$$T_e = \frac{1}{2} i^2 \frac{dL(\theta, i)}{d\theta} \tag{6}$$

Based on (6), and the fact that the phase inductance $L(\theta, i)$ is constructively defined for an existing motor, the shape of the torque profile relies on the current profile. Therefore, one can use the time-efficient model developed in the previous

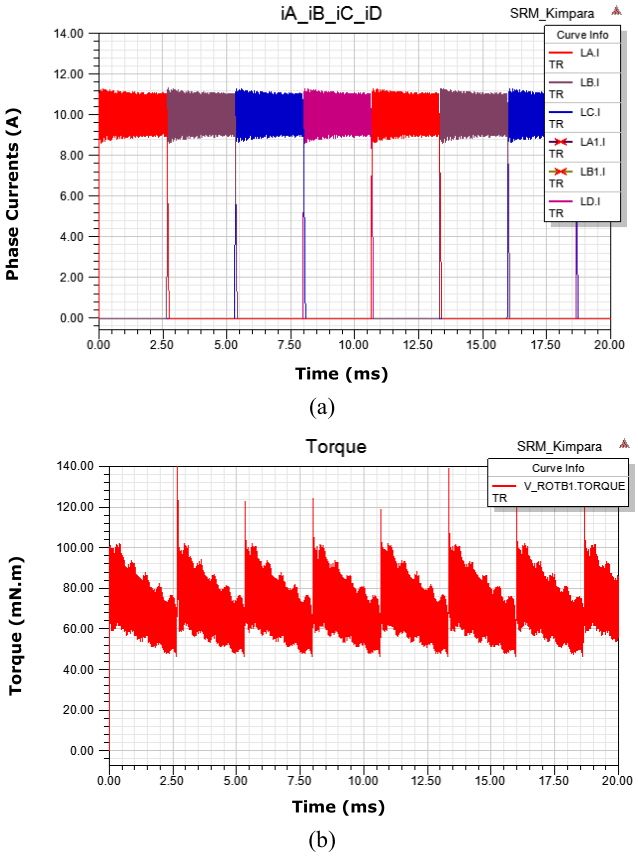

FIGURE 5. Conventional square wave excitation. (a) Phase currents. (b) Resultant torque.

section and equations 3–5 to search for a current profile that minimizes the torque ripple factor.

In SRM, the torque ripple is caused not only because of the commutation from one phase to the next but also due to the reduction in the magnitude of the torque generated as the rotor approaches complete alignment with the stator pole (nonlinear magnetization characteristic).

Mathematically, the torque ripple factor ΔT (in percentage) is expressed by (7):

$$\Delta T = \frac{(T_{max} - T_{min})}{T_{avg}} \cdot 100\% \tag{7}$$

Apart from the electromagnetic characteristics of each particular machine, the control scheme also plays an important role in torque ripple generation. For low-speed operation (up to rated speed), the hysteresis current control is commonly adopted due to its simplicity and fast response.

In such a control strategy, the phase current excitation approaches a square-shaped waveform, and this kind of excitation normally results in torque ripple.

To assess the torque ripple factor using the conventional hysteresis current control, a co-simulation model (Fig. 4) developed in ANSYS Simplorer was used to simulate the SRM operation at 940 rpm. Fig. 5(a) shows the phase currents' waveforms with a reference value of 10 A and a conduction angle of 15° (stroke angle). The sampling frequency

is 1 MHz, and the current controller was set up to a hard-chopping mode with a 2 A hysteresis band. Fig. 5(b) illustrates the resulting torque, where the presence of ripples is notable.

Hence, aiming to minimize the torque ripple factor, an optimization algorithm has been proposed to shape the reference phase current waveforms. The optimization routine used is based on [16], where at a specific rotor position, a current excitation value is applied in the FRM model, and the output torque is calculated and compared with the desired torque. Later, a small perturbation is applied to the tested current value, and the torque is re-calculated and compared with the former value to verify which current value is more beneficial. In each step, the optimal current value is the one that better satisfies the objective function given by (8):

$$J(i) = \left(T - T_{avg}\right)^2 \tag{8}$$

where T is the calculated torque in each iteration and T_{avg} denotes the desired load torque.

Finding an optimum solution for practical problems, such as the minimization of torque ripple through current shaping, raises critical challenges because the function to be optimized, in general, has one or more of the following features: non-differentiable, non-convex feasible space, discrete feasible space, mixed variables (discrete, continuous), large dimensionality, multimodal, and so on. Although gradient-based optimizers are powerful and popular, they do not work for the aforementioned type of problems. For these reasons, non-derivative methods, or zeroth-order methods, that are based on the values of the function, and not on its derivative, are used. In this work, the minimization of the torque ripple was done in Matlab, using the built function *fminsearch* algorithm from the optimization toolbox. This function is based on the Nelder–Mead Simplex.

During the SRM operation, each phase is active within a specific angle range (θ_{on} and θ_{off}) with respect to the magnetic axis of that phase. These angles depend on machine geometry, control strategy, and operating point, therefore, optimizing the current waveform would result in different profiles according to these angles. The proposed algorithm can be applied to different angles, selected according to the operation point, including overlapping excitation of adjacent phases. Fig. 6 shows the phase current profile computed after running the optimization procedure considering the same on and off angles as in Fig. 5. The overall process to generate the optimal phase current reference took approximately 3 minutes. By analyzing the current waveform shown in Fig. 6, one can note that when the torque decreases due to the change in the inductance slope (close to the turn-off), a higher phase current command is needed to produce the necessary torque. Moreover, the obtained profile is compatible with the reported finds in the literature, as in [9]. Increasing the current in commutation phases will maintain the average torque, however at the expense of a higher copper loss.

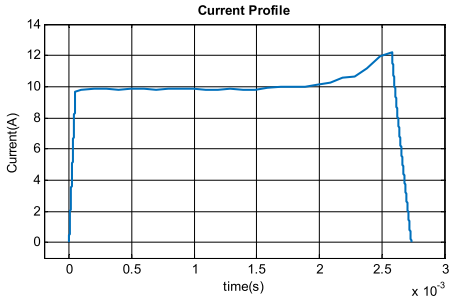

FIGURE 6. Optimized reference phase current profile.

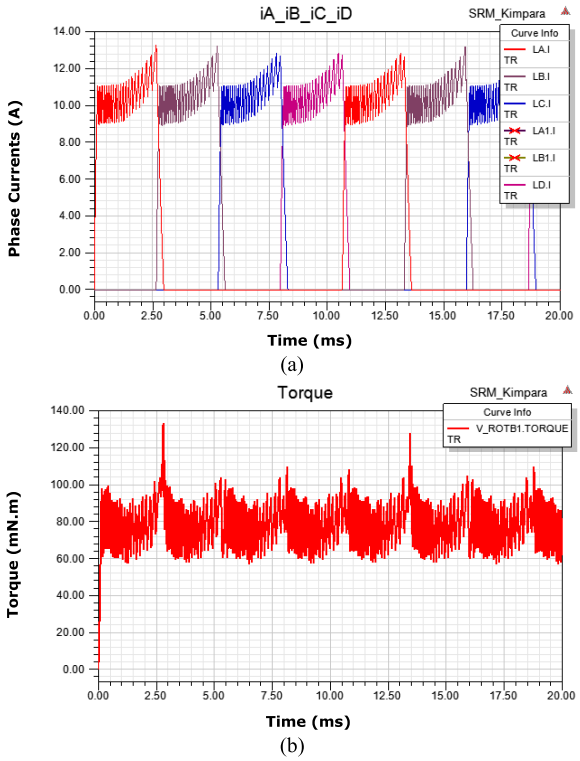

FIGURE 7. Simulation results. (a) Optimized phase currents. (b) Resultant torque.

A. SIMULATION RESULTS

The optimized reference current was imported and simulated in the Simplorer software. Fig. 7 depicts the phase currents and the resultant torque using the proposed current waveform at the same speed as before (940 rpm). As observed, the proposed current excitation generates a smooth torque profile in comparison with the conventional square-wave excitation.

B. EXPERIMENTAL RESULTS

The proposed method for torque ripple mitigation has been assessed experimentally in this section. Fig. 8 shows the test bench where an in-line rotary torque meter (Himmelstein model MCRT 48001V(1-2)) was installed between the target SRM and a PMDC machine acting as load (generator mode). The running speed was set to approximately 170 rpm because the dynamic measurement of torque needs to be accomplished at a low speed due to the torque sensor bandwidth

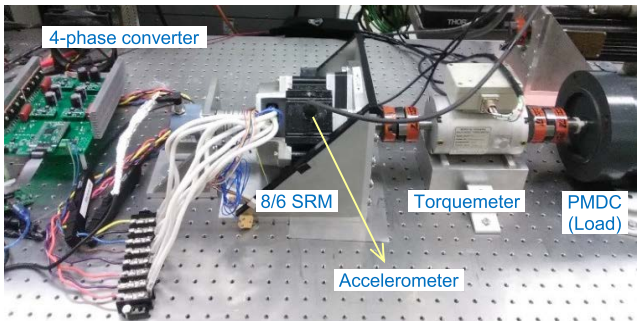

FIGURE 8. Experimental test bench.

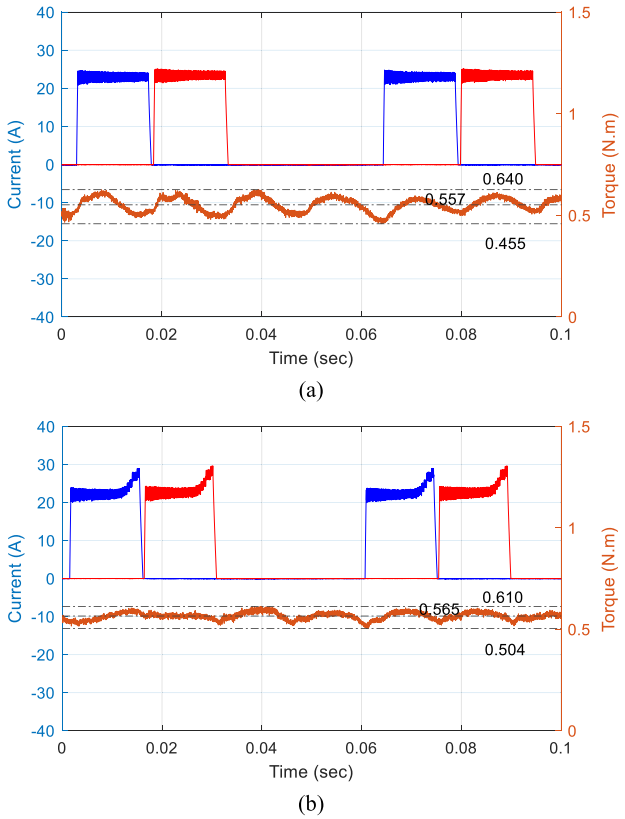

FIGURE 9. Experimental results at 170 rpm and 0.56 Nm. (a) Phase currents and torque profile applying conventional excitation. (b) Phase currents and torque profile with optimized excitation.

and also to reduce the impact of the mechanical coupling in the drive train. Moreover, the torque ripple is particularly harmful at low speeds. The load torque was approximately 0.56 Nm, and the SRM drive consisted of an asymmetric bridge converter controlled by a DSP 28379S.

Fig. 9(a) shows the experimental results obtained with the conventional square flat-top current waveform. The current controller is operating in hard-chopping mode. For this tested condition, the measured torque presents a ripple factor of 33%. The optimized current profile is then tested under the same speed and load conditions, obtaining the results shown in Fig. 9(b). As can be noticed, the proposed current profile successfully reduces the torque ripple to approximately 18.7%.

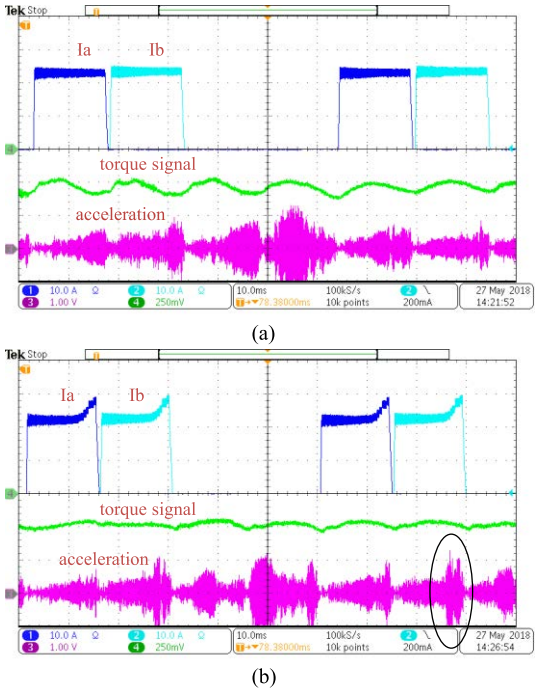

FIGURE 10. Vibration measurement (10.2 mV/m/s^2) at 170 rpm and 0.56 Nm. (a) Conventional square-wave current excitation. (b) Optimized current excitation.

Albeit the torque ripple minimization has been confirmed, the proposed current profile might adversely affect the motor structural vibration. This is expected because, to reduce torque pulsation without penalizing the average torque, the magnitude of the current in the vicinity of the commutation region (i.e., turn-off region) need to increase. Accordingly, radial forces acting on the stator frame will increase as the current magnitude increases. Since the radial forces are considered the primary source of SRM structural vibration, the optimal current profile for torque ripple mitigation will inevitably give rise to a higher vibration and corresponding acoustic noise.

To overcome this problem, the following section presents a technique to attenuate the structural vibration.

V. VIBRATION ANALYSIS AND ACTIVE CANCELLATION

The effectiveness of the proposed control strategy in reducing the torque ripple has been demonstrated by simulation and experimental results. However, the effect of this new current on the structural vibration is also investigated by measuring the acceleration of the stator frame before and after the torque optimization. Fig. 8 shows the accelerometer (PCB piezotronics model 623C01) placed on the stator housing and Fig. 10 illustrates the experimental results. The operation point is the same as previously analyzed (170 rpm and 0.56 Nm), however, the measured acceleration (signal in magenta) reaches higher magnitudes in the region close to the turn-off angle when the optimized current is impressed.

In order to quantify the overall vibration, the measured acceleration was converted to the frequency domain and the

corresponding total energy W, deduced from the energy spectral density and Parseval's theorem, was calculated over a wide range of frequencies [24]:

$$W = \int_0^{f\,max} a\,(f)\,.a^*\,(f)\,df \tag{9}$$

where $a(f)$ stands for the magnitude of the acceleration (FFT) at the frequency f and $a^*(f)$ is the complex conjugate of $a(f)$. Using (9), a comparison between the results in Fig. 10(a) and Fig. 10(b) reveals that the vibration has been increased by 34% considering the frequency ranging up to 20 kHz (audible range).

Therefore, aiming to prevent higher vibration and acoustic noise levels, a second optimization approach based on variable hysteresis current band is proposed. This new optimization will be combined with the optimized reference current depicted in Fig. 6, resulting in a hybrid approach. It is important to highlight that in the simulation and experimental tests covered in section III, only the reference current profile was modified, but the hysteresis limits remained constant (uniform band).

The variable hysteresis band is proposed in order to contribute to the active vibration cancellation. As described in [25], the stator vibration (acceleration $a(t)$) can be estimated by convolving the derivative of the input power with the mechanical impulse response (MIR) corresponding to the actual rotor position (θ_r):

$$a\,(t) = \frac{dP}{dt} * h_a\,(i, \theta_r) \tag{10}$$

where $h_a(i, \theta_r)$ is the mechanical impulse response and $^{dP}/_{dt}$ is the derivative of power given by (11) for constant DC voltage [25]:

$$\frac{dP}{dt} = \sum_{j=1}^{N} 4V_{dc} \cdot i(t)\left(\delta\left(t - t_{j-1}\right) - \delta(t - t_j)\right) \tag{11}$$

the variable t represents the turn-on and turn-off instants (switching). During the turn-on state, the radial component of the force will arise from the attraction between the rotor and stator poles, hence creating a microscopic deformation (contraction) in the stator frame. Later, when the excitation is removed, the stator relaxes and due to the elastic properties of the material, the stator frame will expand. Fig. 11(a) illustrates the vibration mechanism according to the signal captured by the accelerometer on the top of the stator frame during a pulse of voltage excitation (impulse). Furthermore, it is important to notice that the vibration continues to propagate even after the electrical excitation is removed. Acoustic noise is a by-product of this process.

Accordingly, the hysteresis current control naturally consists of a sequence of switchings in order to keep the current within an upper and lower limit. Hence, at every switching (step-change in electrical input) a new vibration is introduced, and will be superimposed with the remaining vibration caused by previous switchings. Based on that, the proposed optimization consists of adjusting the hysteresis band aiming to modify the switching instants. As shown in Fig. 11(b),

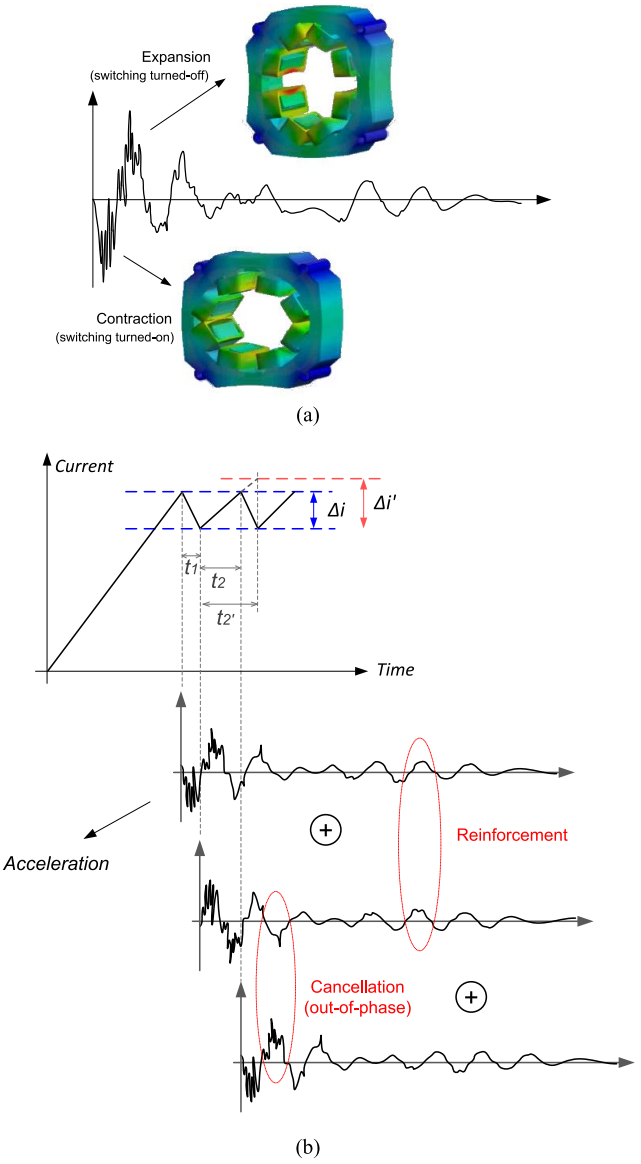

FIGURE 11. Vibration mechanism. (a) Vibration due to a single switching and one of the stator vibration modes. (b) Superposition of individual vibrations introduced after a sequence of switching.

depending on the switching instants, which are indirectly defined by the band limits (Δi), the introduced vibration is shifted (t_2) and may produce a reinforced effect with the previous vibration in some instants, whereas at other instants there may be some active cancellation taking place. Therefore, there might exist an ideal hysteresis band ($\Delta i'$) that enhances the cancellation effect resulting in lower net vibration.

The active vibration cancellation based on switching optimization has been investigated in [26]; however, every single switching has to be optimized within the conduction period, resulting in a lot of stored data in the lookup tables and precisely controlled processing. Herein, the proposed optimization is accomplished only in the vicinity of alignment, where the radial forces are critical. Moreover, instead of

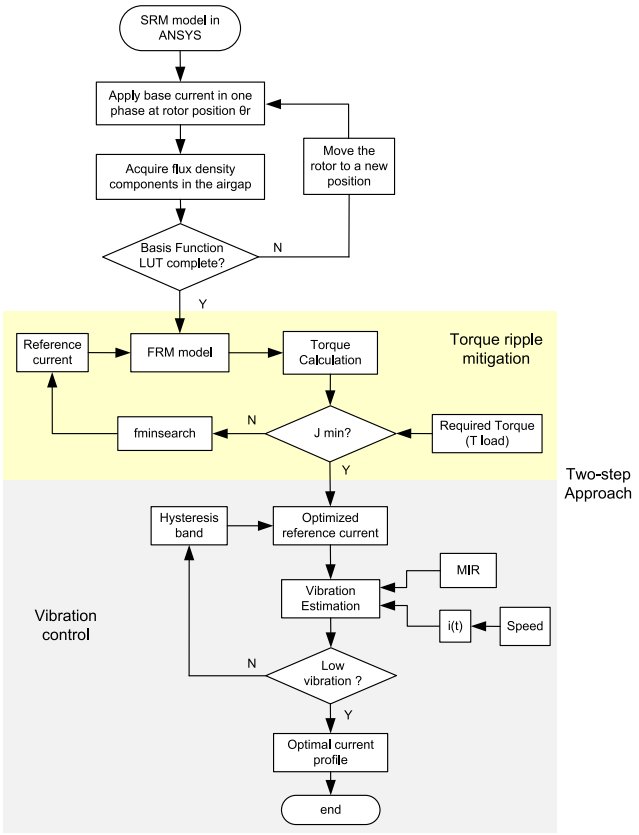

FIGURE 12. Flowchart diagram including the two-step hybrid approach.

TABLE 2. Values of hysteresis band in each $\Delta\theta$ region.

Hysteresis band (Δi)				
HB1	HB2	HB3	HB4	HB5
2.05 A	0.95 A	1.85 A	1.41 A	1.12 A

optimizing all the switching instants, it has been observed that varying the hysteresis band (a set of switching) is also effective and simpler.

A Matlab routine was developed to search for the optimal hysteresis band. Firstly, impulse responses at various rotor positions were captured, spanning from the unaligned to the aligned position, and stored in a lookup table [26]. The impulse response was normalized by the peak current. Afterward, to estimate the vibration for a specific condition, the computed acceleration depended on the current value at the switching instant (see eq. (10) and (11)), hence the instantaneous current value was calculated using the analytical expression given by (12):

$$i\,(t) = i_0.e^{-\frac{t}{\tau}} + \frac{V_{dc}}{R_{eq}}.\left(1 - e^{-\frac{t}{\tau}}\right) \tag{12}$$

where: $R_{eq} = R_s + \omega\frac{dL}{d\theta}$ and $\tau = \frac{L(i,\theta)}{R_{eq}}$

The incremental inductance of (12) was obtained from experimental flux linkage measurement. A flowchart illustrating the proposed two-step approach is presented in Fig. 12. To incorporate the AVC, the region in the current profile

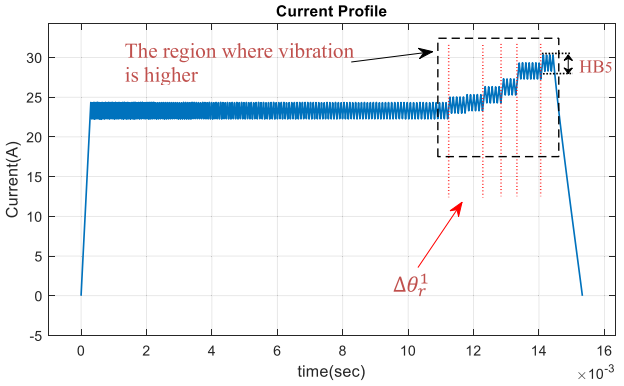

FIGURE 13. Detail of the current segment to be optimized, divided into 5 regions.

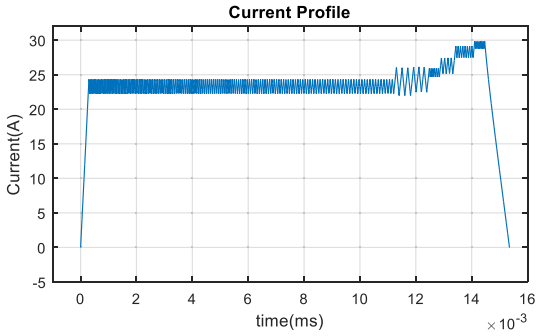

FIGURE 14. Hybrid optimized current profile for torque ripple mitigation and AVC.

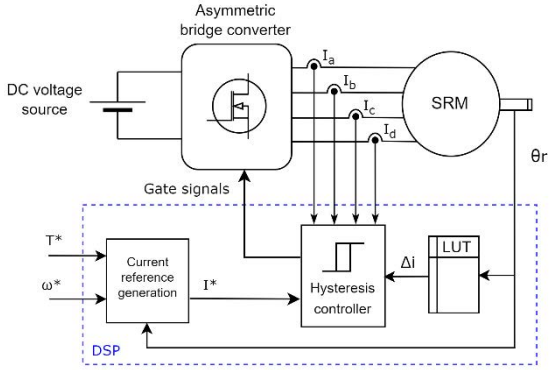

FIGURE 15. Control block diagram.

where the magnitude has been increased (to compensate for the torque) was divided into five small regions, as shown in Fig. 13. For each of these regions, a different hysteresis band (HB) has been optimally defined to reduce the radial vibration. The SRM radial vibration was estimated using (10), considering initial values for the HB in $\Delta\theta_r^1, \Delta\theta_r^2, \ldots \Delta\theta_r^5$. The Matlab toolbox *optimtool* was then used to modify the value of the HB in each $\Delta\theta_r$ region iteratively and recalculate the vibration, in an attempt to find out which value results in a lower overall vibration. Table 2 summarizes the HB found for each region and Fig. 14 shows the theoretical resultant current profile obtained after the two-step optimization procedure. One can clearly notice that HB is not uniform for the entire

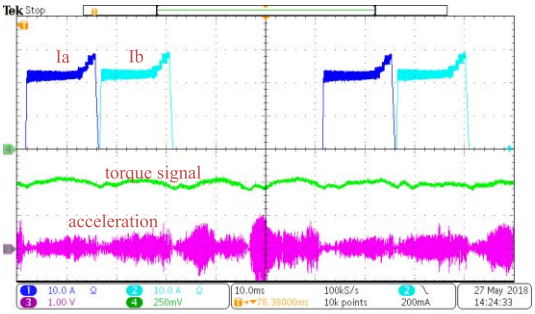

FIGURE 16. Torque and vibration performance due to the proposed current profile excitation at 170 rpm and 0.56 Nm.

TABLE 3. Performance comparison – 170 rpm.

Current Profile	Torque		Vibration	
	Ripple factor (eq. 7)	Comparison with conventional	Total Energy (eq. 9)	Comparison with conventional
Square with uniform HB (conventional)	33.2%	--	$2.28e^{10}$J	--
Optimized with uniform HB	18.7%	44% lower	$3.05e^{10}$J	33.7% higher
Optimized with variable HB	19.2%	42% lower	$1.86e^{10}$J	18.4% lower

conduction period. Fig. 15 illustrates the control diagram implemented in the DSP to drive the SRM with the proposed method.

The experimental results for the motor operating with the optimized current profile and adapted hysteresis band are shown in Fig. 16. The operation conditions are the same as previously tested. All the phases exhibited a reduction in the vibration signal. The vibration captured by the sensor had a different signature depending on whether the exciting phase was closer or farther from the accelerometer location.

Table 3 presents a comparative analysis in terms of torque ripple and vibration between the three tested current profiles. In addition, Fig. 17 presents a more detailed experimental comparison between the conventional current waveform (square-wave with uniform HB), the current profile that minimizes the torque ripple (Fig. 6 with uniform HB), and the current profile optimized with the proposed two-step approach (Fig. 14). Notably, with conventional excitation, the torque signal (green) presents higher oscillation, and the vibration (magenta) naturally increases as the rotor moves to come in alignment with the stator pole. After the torque optimization, the magnitude of torque oscillation is reduced; however, the vibration becomes higher when compared to the conventional case. Nonetheless, after incorporating the variable hysteresis band, the commanded current is suitable to give rise to a low-ripple torque, and simultaneously, not only prevents the vibration increase but further reduces it. The vibration signal analysis in the frequency domain is shown in Fig. 18. One can observe that the optimized current

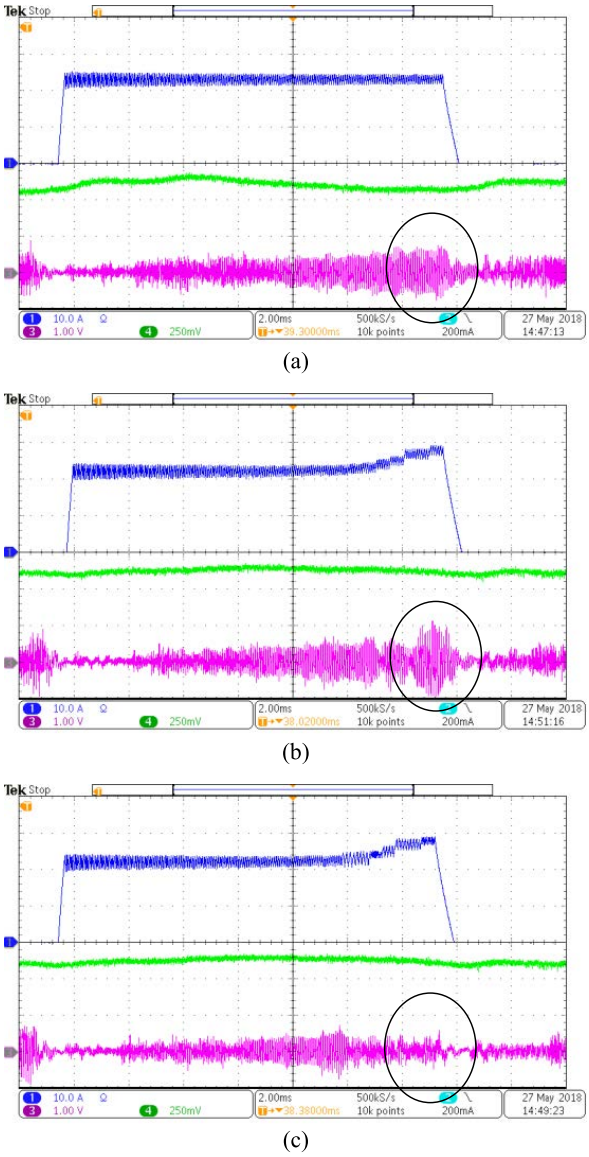

FIGURE 17. Experimental torque ripple and vibration comparison at 178 rpm and 0.3 Nm, with phase current in blue color, torque in green color (440.2 mV/Nm) and vibration in magenta (10.2 mV/m/s^2). (a) Conventional square-wave current excitation with uniform hysteresis band. (b) Optimized excitation for torque ripple reduction with uniform hysteresis band. (c) Current profile with a hybrid approach for torque ripple reduction and AVC.

profile with uniform HB has resulted in additional excitation in the vibration modes associated with the natural frequencies around 2.1 kHz and 11.6 kHz. Although the vibration component in 13.2 kHz has decreased, the overall vibration (eq. 9) has increased by 19%. On the other hand, the proposed current profile with the variable hysteresis band produces a vibration in which the frequency components of 2.1 kHz and 11.6 kHz have been attenuated. In addition, the component of 13.2 kHz is lower than the case of the conventional excitation.

In general, one can observe that the negative effect in the vibration response due to the increase in current amplitude has been softened by the adaptive hysteresis band. The merit of this approach is the fact that radial vibration is an inherent

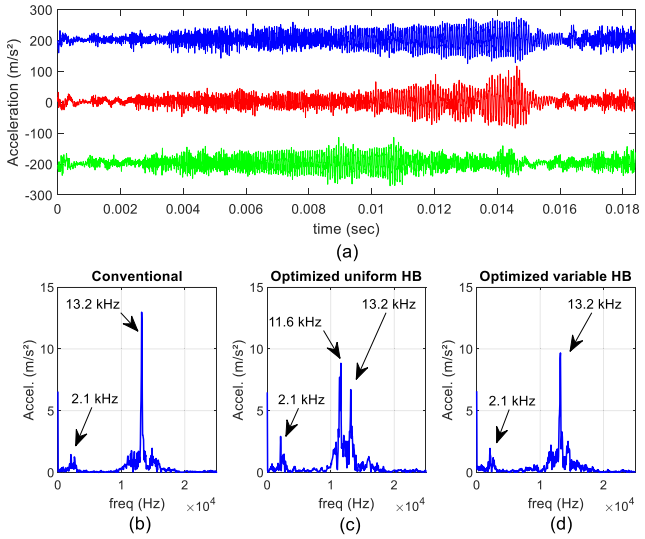

FIGURE 18. Comparison of the measured acceleration in frequency domain. (a) Acceleration in time domain. (b) Acceleration in frequency domain due to conventional excitation. (c) Acceleration in frequency domain due to optimized current with uniform HB. (d) Acceleration in frequency domain due to optimized current with variable HB.

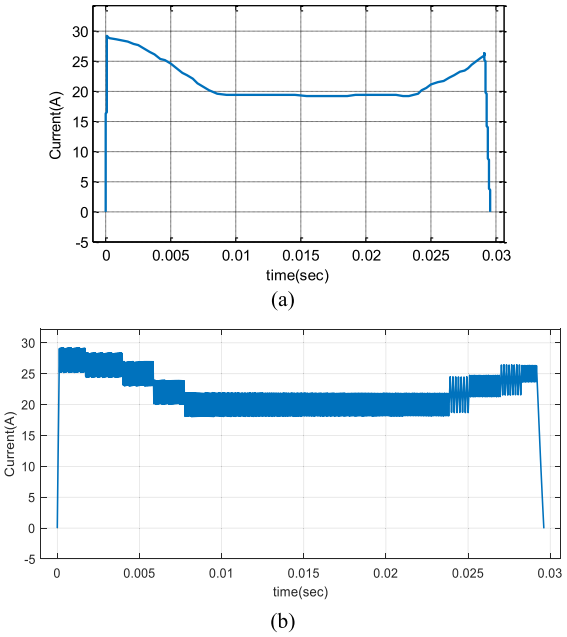

FIGURE 19. Optimized reference current profile for torque ripple and vibration mitigation at 80 rpm. (a) First-step approach: torque ripple reduction. (b) Second-step approach: active vibration cancellation.

characteristic of SRM; thus, instead of trying to avoid or shape it, which may penalize the torque generation, one can take the advantage of the active cancellation to suppress the vibration mitigating the undesirable effects of noise.

Reference currents are shaped depending on the driving angles. Thus, in order to further verify the effectiveness of the proposed method, another operation point has been tested with the firing angle closer to the unaligned position. The off-line current shaping routine has been performed, yielding the reference current profile shown in Fig. 19(a). Once more, one can observe that to reach a low-torque ripple factor, the phase current presents an AC component to compensate for

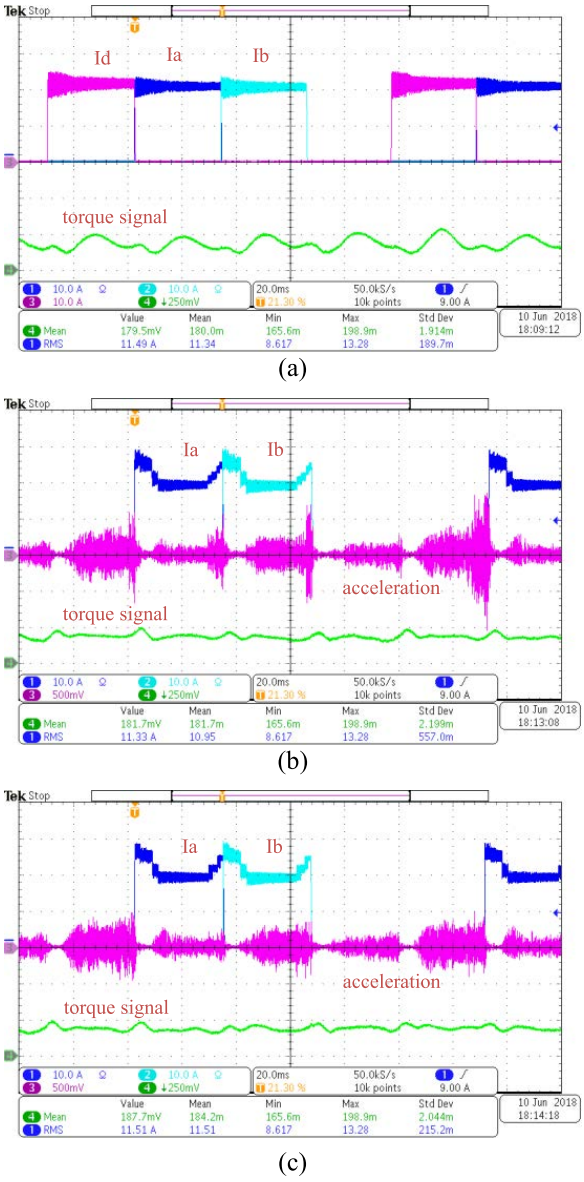

FIGURE 20. Torque (440.2 mV/Nm) and vibration (10.2 mV/m/s^2) performance comparison for different current excitations at 80 rpm and 0.4 Nm. (a) Conventional flat-top phase current profile. (b) Optimized current profile with uniform hysteresis band. (c) Hybrid approach for torque ripple and vibration.

the non-linearity in the static torque profile. Subsequently, the variable HB optimization has been included resulting in the current excitation shown in Fig. 19(b).

Experimentally, Fig. 20 shows the oscilloscope screenshot for the SRM operating at 80 rpm and 0.4 Nm. In Fig. 20(a), one can note a pulsating torque profile with 70% ripples, whereas in Fig. 20(b) the torque oscillation has been attenuated by 43%, but with the vibration increasing to around 30%. On the other hand, the excitation current, which encompasses the variable hysteresis band (Fig. 20(c)), properly minimizes the torque ripple while the vibration is controlled at lower levels. Comparing the hybrid approach with the typical square wave excitation, the torque ripple has been reduced by 42.6%, and the stator vibration has been softened by 22%.

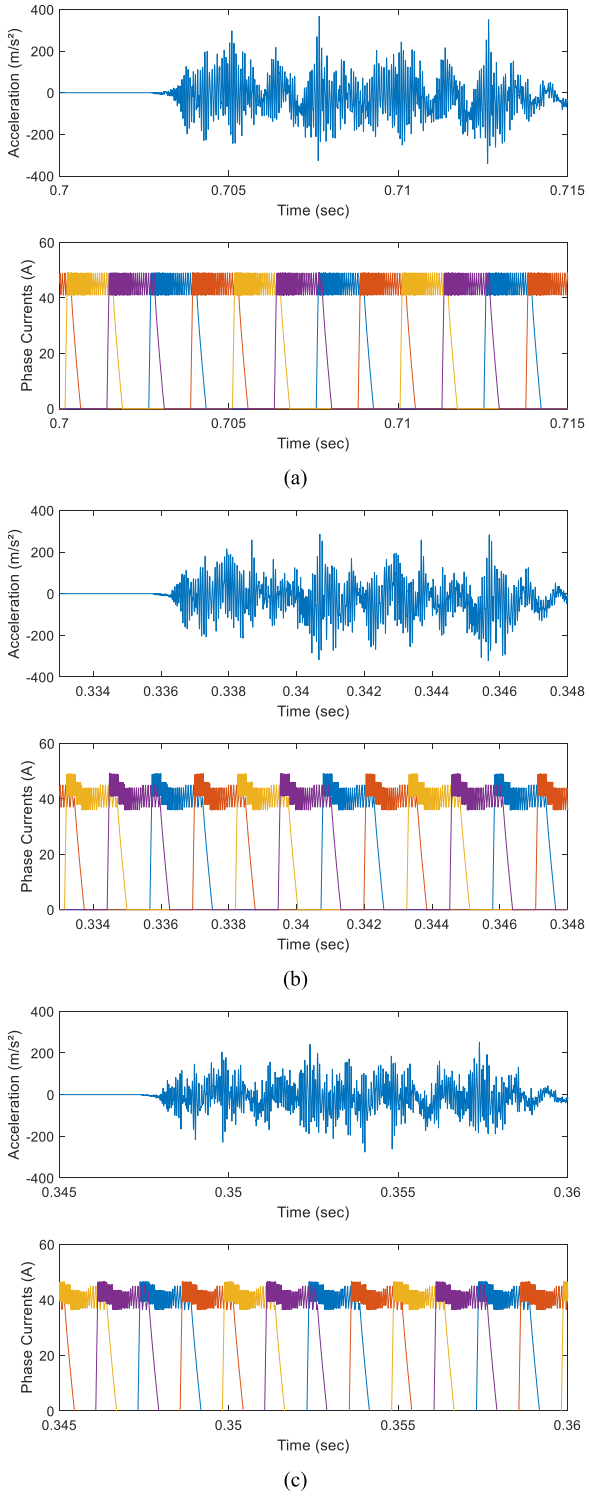

FIGURE 21. Vibration estimation for the SRM operating under 2000 rpm and 1 Nm. (a) Square current – uniform hysteresis band. (b) Optimized current profile – uniform hysteresis band (c) Optimized current profile – variable hysteresis band.

It is worth mentioning that although the current profile shows higher magnitudes at the beginning of the conduction period, it was not necessary to modify the HB in this region because the vibration is the most severe close to the aligned position. Moreover, the number of adaptive intervals will depend on the machine characteristics and the operating

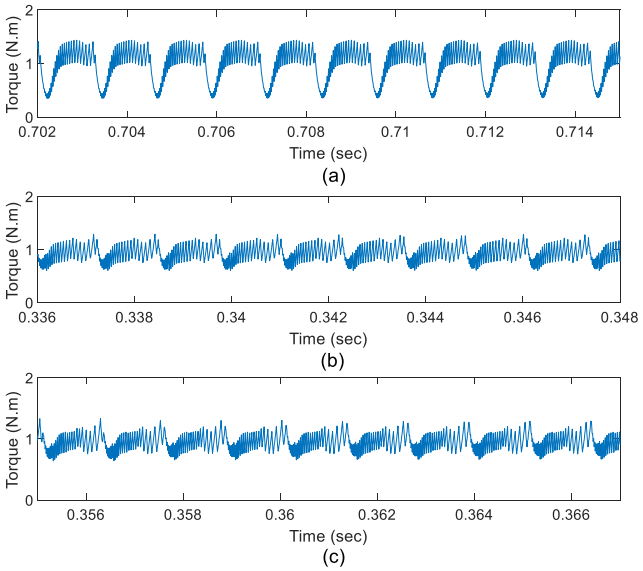

FIGURE 22. Torque profile for the SRM operating under 2000 rpm and 1 Nm. (a) Square current with uniform hysteresis band excitation. (b) Optimized current profile with uniform hysteresis band excitation. (c) Optimized current profile with variable hysteresis band excitation.

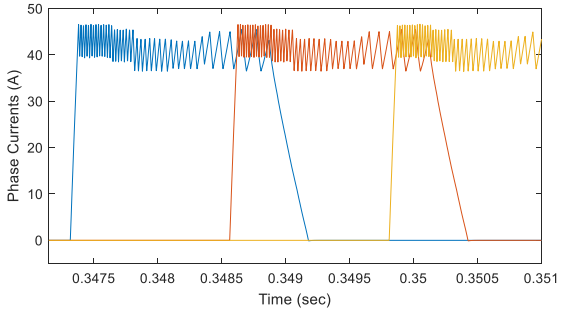

FIGURE 23. Phase currents profile for low torque ripple and reduced radial vibration.

point, i.e., the angular position where the current starts to increase to compensate for the torque dip.

As one can notice, the experimental tests have been conducted under low torque conditions. The reason for that is the limitations of the experimental setup, mainly regarding the current sensor (measures up to 30 A). However, the proposed approach can be applied to any operation point below the base speed.

To validate the effectiveness of the method for the SRM operating under 2000 rpm and 1 Nm, simulation results are presented in Fig. 21, where the stator vibration has been estimated using equation (10). It is possible to note that for the square phase current excitation with a uniform hysteresis band, high vibration level is observed, especially in the region where the adjacent phase currents are overlapped.

Despite the overlap, the torque profile still may present a high ripple factor (Fig. 22), which can be further improved through current shaping. In this regard, Fig. 21(b) and Fig. 22(b) show the results for such optimized excitation. The simulation results in Fig. 21(b) demonstrated that the overall vibration is worsened when compared to Fig. 21(a). Therefore, by controlling the hysteresis band it is possible to reduce the vibration without affecting the torque ripple

TABLE 4. Performance comparison – 2000 rpm (simulated).

Current Profile	Torque		Vibration	
	Ripple factor (eq. 7)	Comparison with conventional	Total Energy (eq. 9)	Comparison with conventional
Square with uniform HB (conventional)	98%	--	$1.25e^{13}$J	--
Optimized with uniform HB	59.3%	39.5% lower	$1.71e^{13}$J	36.8% higher
Optimized with variable HB	60%	38.7% lower	$1.03e^{13}$J	17.6% lower

benefits. The results in Fig. 21(c) and Fig. 22(c) confirm this statement. Fig. 23 shows the current profile after the two-step optimization considering the simulated condition.

One can notice that the vibration signature may present some differences according to operation point (load and speed). That happens because the slew rate of current will change within the dwell angle depending on the speed (back-emf effect) and the inductance (commutation angle effect) which will naturally shift the switching times under hysteresis current control, resulting in a net vibration slightly different in time domain. Nevertheless, it is important to emphasize that in all cases, optimal tunning the hysteresis band will result in lower vibration when compared with the conventional current profile and optimized profile with a uniform hysteresis band. Table 4 summarizes the quantitative analysis for the results shown in Fig. 21.

VI. CONCLUSION

Albeit the current profiling is an effective and commonly adopted strategy for minimizing the torque ripple in SRM drives, most of the studies in the literature only care about the torque profile when using such a strategy and do not investigate the effects of the current profiling from the vibration standpoint. This paper not only demonstrated that there exists an adverse effect of current profiling but also introduced a novel two-step technique to derive optimal current waveforms that consists of associating the reference current profiling technique to an adaptive hysteresis band controller aiming to reduce torque ripple without increasing vibration. The torque ripple factor has been improved for two different operating points while the AVC effectively suppressed the additional radial vibration. The experimental verification has demonstrated the feasibility of the proposed solution at lower speeds. The control strategy in all operating region, including the transient conditions, will be future work.

REFERENCES

[1] E. Bostanci, M. Moallem, A. Parsapour, and B. Fahimi, "Opportunities and challenges of switched reluctance motor drives for electric propulsion: A comparative study," *IEEE Trans. Transport. Electrific.*, vol. 3, no. 1, pp. 58–75, Mar. 2017, doi: 10.1109/TTE.2017.2649883.

[2] B. Howey, B. Bilgin, and A. Emadi, "Design of an external-rotor direct drive E-bike switched reluctance motor," *IEEE Trans. Veh. Technol.*, vol. 69, no. 3, pp. 2552–2562, Mar. 2020, doi: 10.1109/TVT.2020.2965943.

[3] A. Spampinato, G. Forte, G. Scelba, and G. De Donato, "A cost-effective switched reluctance motor drive for vacuum cleaners," in *Proc. Int. Symp. Power Electron., Electr. Drives, Autom. Motion (SPEEDAM)*, Sorrento, Italy, Jun. 2020, pp. 36–41.

[4] J. Reinert, K. Inderka, M. Menne, and R. W. D. Doncker, "Optimizing performance in switched-reluctance drives," *IEEE Ind. Appl. Mag.*, vol. 6, no. 4, pp. 63–70, Jul. 2000, doi: 10.1109/2943.847917.

[5] Z. Lin, D. S. Reay, B. W. Williams, and X. He, "Torque ripple reduction in switched reluctance motor drives using B-spline neural networks," *IEEE Trans. Ind. Appl.*, vol. 42, no. 6, pp. 1445–1453, Nov. 2006, doi: 10.1109/TIA.2006.882671.

[6] T. Zhao, J. Li, and X. Gui, "An offline iterative torque optimization for extended-speed control of switched reluctance motor drives," in *Proc. 22nd Int. Conf. Electr. Mach. Syst. (ICEMS)*, Harbin, China, Aug. 2019, pp. 1–6.

[7] M. Shirahase, S. Morimoto, and M. Sanada, "Torque ripple reduction of SRM by optimization of current reference," in *Proc. Int. Power Electron. Conf. (ECCE ASIA)*, Sapporo, Japan, Jun. 2010, pp. 2501–2507.

[8] B. P. Reddy, J. R. Vemula, and S. Keerthipati, "Torque ripple minimisation of switched reluctance motor using sense coils," *IET Elect. Power Appl.*, vol. 14, no. 4, pp. 614–621, Apr. 2020, doi: 10.1049/iet-epa.2019.0787.

[9] R. Mikail, I. Husain, Y. Sozer, M. S. Islam, and T. Sebastian, "Torque-ripple minimization of switched reluctance machines through current profiling," *IEEE Trans. Ind. Appl.*, vol. 49, no. 3, pp. 1258–1267, May 2013, doi: 10.1109/TIA.2013.2252592.

[10] L. Feng, X. Sun, X. Tian, and K. Diao, "Direct torque control with variable flux for an SRM based on hybrid optimization algorithm," *IEEE Trans. Power Electron.*, vol. 37, no. 6, pp. 6688–6697, Jun. 2022, doi: 10.1109/TPEL.2022.3145873.

[11] Z. Xia, B. Bilgin, S. Nalakath, and A. Emadi, "A new torque sharing function method for switched reluctance machines with lower current tracking error," *IEEE Trans. Ind. Electron.*, vol. 68, no. 11, pp. 10612–10622, Nov. 2021, doi: 10.1109/TIE.2020.3037987.

[12] S. R. Mousavi-Aghdam, A. Moradi, and A. M. Dolatkhah, "Torque ripple reduction of switched reluctance motor using improved torque sharing functions," in *Proc. Iranian Conf. Electr. Eng. (ICEE)*, Tehran, Iran, May 2017, pp. 1043–1047.

[13] M. Kawa, K. Kiyota, J. Furqani, and A. Chiba, "Acoustic noise reduction of a high-efficiency switched reluctance motor for hybrid electric vehicles with novel current waveform," *IEEE Trans. Ind. Appl.*, vol. 55, no. 3, pp. 2519–2528, May/Jun. 2018.

[14] A. D. Callegaro, B. Bilgin, and A. Emadi, "Radial force shaping for acoustic noise reduction in switched reluctance machines," *IEEE Trans. Power Electron.*, vol. 34, no. 10, pp. 9866–9878, Oct. 2019, doi: 10.1109/TPEL.2019.2891050.

[15] C. Ma, L. Qu, R. Mitra, P. Pramod, and R. Islam, "Vibration and torque ripple reduction of switched reluctance motors through current profile optimization," in *Proc. IEEE Appl. Power Electron. Conf. Expo. (APEC)*, Long Beach, CA, USA, Mar. 2016, pp. 3279–3285.

[16] M. Kimpara, P. Ribeiro, J. O. P. Pinto, D. Andrade, B. Fahimi, L. da Silva, B. Ozpineci, and M. Kiani, "Improvement in torque profile of switched reluctance motors," in *Proc. IEEE 26th Int. Symp. Ind. Electron. (ISIE)*, Edinburgh, U.K., Jun. 2017, pp. 309–314.

[17] J. Liang, B. Howey, B. Bilgin, and A. Emadi, "Source of acoustic noise in a 12/16 external-rotor switched reluctance motor: Stator tangential vibration and rotor radial vibration," *IEEE Open J. Ind. Appl.*, vol. 1, pp. 63–73, 2020, doi: 10.1109/OJIA.2020.3011395.

[18] M. Kimpara, S. Wang, R. Reis, J. Pinto, M. Moallem, and B. Fahimi, "On the cross coupling effects in structural response of switched reluctance motor drives," *IEEE Trans. Energy Convers.*, vol. 34, no. 2, pp. 620–630, Jun. 2019, doi: 10.1109/TEC.2018.2863199.

[19] C. Gan, J. Wu, Q. Sun, W. Kong, H. Li, and Y. Hu, "A review on machine topologies and control techniques for low-noise switched reluctance motors in electric vehicle applications," *IEEE Access*, vol. 6, pp. 31430–31443, 2018, doi: 10.1109/ACCESS.2018.2837111.

[20] C. Lin, W. Wang, M. McDonough, and B. Fahimi, "An extended field reconstruction method for modeling of switched reluctance machines," *IEEE Trans. Magn.*, vol. 48, no. 2, pp. 1051–1054, Feb. 2012, doi: 10.1109/TMAG.2011.2172917.

[21] D. Wu, S. D. Pekarek, and B. Fahimi, "A voltage-input-based field reconstruction technique for efficient modeling of the fields and forces within induction machines," *IEEE Trans. Ind. Electron.*, vol. 57, no. 3, pp. 994–1001, Mar. 2010, doi: 10.1109/TIE.2009.2035466.

[22] S. J. Salon, *Finite Element Analysis of electrical Machines*. New York, NY, USA: Springer, 1995.
[23] R. Krishnan, *Switched Reluctance Motor Drives: Modeling, Simulation, Analysis, Design and Applications*. Boca Raton, FL, USA: CRC Press, 2001.
[24] A. Kolli, G. Krebs, X. Mininger, and C. Marchand, "Impact of command parameters on efficiency, torque ripple and vibrations for switched reluctance motor," in *Proc. XXth Int. Conf. Electr. Mach.*, Sep. 2012, pp. 2975–2980.
[25] C. Lin and B. Fahimi, "Prediction of radial vibration in switched reluctance machines," *IEEE Trans. Energy Convers.*, vol. 28, no. 4, pp. 1072–1081, Dec. 2013, doi: 10.1109/TEC.2013.2285165.
[26] M. L. M. Kimpara, S. Wang, C. A. Caicedo-Narvaez, T. Chen, J. O. P. Pinto, L. E. Borges da Silva, M. Moallem, and B. Fahimi, "Active cancellation of vibration in switched reluctance motor using mechanical impulse response method," *IEEE Trans. Energy Convers.*, vol. 34, no. 3, pp. 1358–1368, Sep. 2019.

MARCIO L. M. KIMPARA (Member, IEEE) was born in Jales, Brazil, in May 1986. He received the B.S. and M.S. degrees in electrical engineering from the Federal University of Mato Grosso do Sul (UFMS), Campo Grande, Brazil, in 2009 and 2012, respectively, and the Ph.D. degree from the Federal University of Itajubá, Itajubá, Brazil, in 2018. He is currently a Professor with the Department of Electric Engineering, UFMS. His research interests include power electronics, renewable energy, and electric machines and drives.

RENATA R. C. REIS (Student Member, IEEE) was born in Campo Grande, Brazil, in August 1993. She received the B.S. and M.S. degrees in electrical engineering from the Federal University of Mato Grosso do Sul (UFMS), Campo Grande, in 2019 and 2022, respectively. Her research interests include renewable energies, power electronics, electric machines, and artificial intelligence applications.

LUIZ E. B. DA SILVA (Senior Member, IEEE) received the B.S. and M.Sc. degrees in electrical engineering from the Federal University of Itajuba (UNIFEI), Itajuba, Brazil, in 1977 and 1982, respectively, and the Ph.D. degree from the École Polytechnique de Montreal, Montreal, QC, Canada, in 1988. In 1998, he was a Visiting Professor with The University of Tennessee, Knoxville, TN, USA. He is currently a Professor with the Department of Electronic Engineering, UNIFEI, where he is also the Head of Power Electronics. He has supervised more than 30 M.Sc. and Ph.D. theses. He has directed many projects in the field of industrial electronics and coauthored over 200 technical articles. His research interests include power electronics, electronic power systems, power converters, and applications of adaptive and intelligent control in industrial problems.

JOAO O. P. PINTO (Senior Member, IEEE) was born in Valparaiso, Brazil. He received the B.S. degree in electrical engineering from the Universidade Estadual Paulista, Brazil, in 1990, the M.S. degree from the Universidade Federal de Uberlândia, Brazil, in 1993, and the Ph.D. degree from The University of Tennessee, Knoxville, in 2001. He was a Faculty Member at the Federal University of Mato Grosso do Sul (UFMS), Campo Grande, Brazil, from 1994 to 2021, where he also worked as the Dean of the Engineering College, from 2013 to 2017. He was the Founder and the Director of the BATLAB, artificial intelligence applications, power electronics and drives, and energy systems. He has been a Faculty Member of the Federal University of Rio de Janeiro, Rio de Janeiro, Brazil, on leave of absence, since 2021. He is currently a Senior Researcher at the Oak Ridge National Laboratory, Oak Ridge, TN, USA. He has over 200 published papers in journals and conferences proceedings. His research interests include power electronics, artificial intelligence applications, energy systems, electrical machine drives, and among others.

BABAK FAHIMI (Fellow, IEEE) received the B.S. and M.S. degrees (Hons.) in electrical engineering from the University of Tehran, Iran, in 1991 and 1993 respectively, and the Ph.D. degree in electrical engineering from Texas A&M University, in 1999. He has been active in research on electric machines and drives over the past 30 years. He has coauthored over 375 peer-reviewed articles and holds 22 U.S. patents. He has been the advisor for 36 Ph.D. students and 30 M.S. students. He is a fellow of IEEE for his contributions to modeling of adjustable speed motor drives.